A metal-organic framework based on Co(II) and 3-aminoisonicotinate showing specific and reversible colourimetric response to solvent exchange with variable magnet behaviour

O. Pajuelo-Corral [a], S. Pérez-Yáñez [b, c], I.J. Vitorica-Yrezabal [d], G. Beobide [b, c], A. Zabala-Lekuona [a], A. Rodríguez-Diéguez [e], J.M. Seco [a, *], J. Cepeda [a, *]

[a] Departamento de Química Aplicada, Facultad de Química, Universidad Del Pais Vasco (UPV/EHU), 20018 Donostia, Spain
[b] Departamento de Química Orgánica e Inorgánica, Facultad de Ciencia y Tecnología, Universidad Del País Vasco/Euskal Herriko Unibertsitatea (UPV/EHU), 48940 Leioa, Spain
[c] BCMaterials, Basque Center for Materials, Applications and Nanostructures, UPV/EHU Science Park, 48940 Leioa, Spain
[d] School of Natural Sciences, University of Manchester, M13 9PL Manchester, UK
[e] Departamento de Química Inorgánica, Facultad de Ciencias, Universidad de Granada, 18071 Granada, Spain

ARTICLE INFO

ABSTRACT

A versatile metal-organic system consisting of Co-based compounds that show reversible transformations between a 3D metal-organic framework (MOF) of $\{[Co(\mu\text{-}3isoani)_2]\cdot DMF\}_n$ (**1**) formula (where 3isoani = 3-aminoisonicotinato and DMF = dimethylformamide) and a 0D monomeric $[Co(3isoani)_2(H_2O)_4]$ (**2**) complex is reported. These **1** ↔ **2** transformations, triggered by the exposure of the MOF and the monomer-based compound to H_2O and DMF, respectively, involve colour changes from purple (in MOF **1**) to light brown (in monomeric complex **2**), which imbues the system with colourimetric sensing capacity towards these solvents. Despite the high reactivity of the MOF in contact with water, it presents good thermal stability and permanent porosity with a remarkably high CO_2 capture capacity at room temperature (3.35 mmol/g), which is further analysed by *in situ* single-crystal X-ray diffraction. Experimental magnetic properties and CASSCF/NEVPT2 calculations of all compounds reveal distinct slow magnetic relaxations for 3D and 0D compounds.

© 2022 The Author(s). Published by Elsevier Ltd. This is an open access article under the CC BY-NC-ND license (http://creativecommons.org/licenses/by-nc-nd/4.0/).

1. Introduction

Metal-organic frameworks (MOFs) can be considered as one of the most exciting compounds in the field of porous materials because of their tuneable and functional porosities that bring about a wide range of properties for specific applications such as gas adsorption and separation, catalysis and even health care [1–7]. In fact, their success in this field is derived from the possibility of not only rendering huge internal specific surface areas but also controlling the voids and chemical functions decorating the surface thanks to a quite well-established rational design of the constituents that build the structure up [8–11]. According to it, the growth of MOFs lies on the principles of reticular chemistry [12], in such a way that the shape and geometry of the structural units formed by the combination of metal ions (or clusters) acting as nodes and organic molecules acting as linkers leads to endless structural diversity with fascinating topologies [13–15]. Among them, the open networks with large available spaces, which allow the co-crystallisation of multiple chemically indistinguishable copies, quite exclusive for these metal-organic materials, have received special attention for their capacity to adapt their pores to the guest molecules [16–18]. This fact, in essence, may open the way for specific discrimination of guests by the framework or even instigate guest-induced transformations because interpenetrated MOFs are prone to dynamics, given their characteristic structural flexibility [19]. At this point, it must be clarified that the willingness of these MOFs to modify their structure does not undoubtedly imply a detriment in their overall stability; what is more, it may become an advantage if the transformation takes place under well-known conditions or in the presence of a specific molecule/medium. In this sense, it is worth

---

* Corresponding authors.
E-mail addresses: josemanuel.seco@ehu.eus (J.M. Seco), javier.cepeda@ehu.eus (J. Cepeda).

O. Pajuelo-Corral, S. Pérez-Yáñez, I.J. Vitorica-Yrezabal et al.

Materials Today Chemistry 24 (2022) 100794

noticing that stability may be evaluated from at least three perspectives: chemical, thermal and mechanical stability, which means that a MOF possessing low chemical stability does not necessarily imply that thermal and mechanical should also be [20].

Be that as it may, when these transformations are accompanied by changes in another property, or trigger a new property, the material may perform as a chemical switch, memory or molecular sensor, which is perhaps one of the most pursued goals in the quest for novel and improved detectors for emerging pollutants and volatile organic compounds (VOCs) [21–23]. In this sense, the metal-organic nature of MOFs is another key aspect that benefits the design and construction of multifunctional molecular materials because various physical properties may coexist, cooperate or compete with each other [24]. In fact, a change in the electronic/magnetic properties of a system can be induced by a controlled rearrangement of the structure, especially when it involves a change in the coordination environment because this modifies the crystal field [25]. With particular regard to magnetoresponsive activity, developing new multifunctional materials that combine magnetism with a second property (electrical conductivity or superconductivity, molecular bistability, etc.) has shown promising applicability in the nascent area of spintronics [26,27]. However, most of them are based on rigid lattices and do not take advantage of the structural flexibility, which could give them a new dimension to the sensing performance [28]. Of particular interest are MOFs that behave as single-molecule magnets (SMMs), which retain a net magnetic moment below a blocking temperature after the exposure to a magnetic field that slowly dissipates because of the existence of an energy barrier, which, in turn, is proportional to the zero-field splitting (zfs) parameters and total spin of the paramagnetic centres [29–31]. The study of MOFs-based magnets with tuneable SMM behaviour is very scarce, and only a few works have been reported [28,30].

In any case, it must not be forgotten that the transduction mechanism is one of the most important points to exploit the sensing applicability of the material. Among all the possibilities, a colour change appreciable by the naked eye is clearly one of the most promising mechanisms to detect the presence/absence of a molecule because it hardly requires additional sophisticated equipment. Although the current bibliography related to MOFs sensing is being coped by luminescent materials, colourimetric sensors performing without the need for photoexcitation devices (generally in the UV range) are even more desired [32,33]. In fact, as summarised in a recent review by Wang and co-authors [34], MOFs, taking advantage of soft structural or compositional changes (in the coordination environment, redox-active chromophoric ligands and/or loading of ions or chromophores in the pores), have been already used as colourimetric sensing platforms towards several cations, anions, VOCs, gases and water. However, the number of these colourimetric sensors is scarce, and none of them exhibits the capacity for sensing some toxic species such as dimethylformamide (DMF) [35], which is among the most widely used products used as industrial solvents and in the production of fibbers, films and surface coatings [36].

With these ideas in mind, and following our recent works on the characterisation of new magnets and multifunctional materials [37–40], in this work, we describe the preparation and performance of two Co-based compounds that behave as naked-eye colourimetric sensors of water/DMF in solid state. The fascinating and unique sensing capacity of the present materials lies on the reversible striking transformation undergone between the MOF and a monomeric complex. A detailed characterisation of their magnetic properties is also included to evaluate the potential utility of the sensors with variable magnetic performance under cryocooling conditions, a field yet to be explored.

2. Materials and methods

Full details on the experimental setup used for the chemical characterisation of the compounds as well as the computational strategy may be found in the Electronic Supplementary Information (ESI, see S1 section).

2.1. Synthesis of {[Co(μ-3isoani)₂]·DMF}ₙ (**1**)

Overall, 0.0291 g of $Co(NO_3)_2 \cdot 6H_2O$ (0.1 mmol) and 0.0138 g of H3isoani (0.1 mmol) were placed in a scintillation vial and dissolved in a DMF:H_2O (2:1) solvent mixture to be then sonicated for few minutes. Then, the vial was placed in an oven for 6 h at 110°C and then slowly cooled down to room temperature. Red cubic single crystals of **1** grown during the cooling step were filtered and washed with DMF several times, yielding 30−35% based on metal. Anal. Calcd for $C_{15}H_{17}CoN_5O_5$ (%): C, 44.35; H, 4.22; N, 17.24. Found: C, 44.55; H, 3.98; N, 17.38.

2.2. Synthesis of [Co(3isoani)₂(H₂O)₄] (**2**)

An aqueous-methanolic solution (2:1, 15 mL) containing H3isoani (0.0276 g, 0.2 mmol) was basified with Et_3N until complete dissolution of the ligand. To the latter, an aqueous solution (2 mL) containing $Co(NO_3)_2 \cdot 6H_2O$ (0.0291 g, 0.1 mmol) was added dropwise under continuous stirring. Immediately, a light brown precipitate corresponding to **2** was formed, which was filtered and washed with water and methanol. Yield: 75−80% (based on metal). Anal. Calcd (%) for $C_{12}H_{18}CoN_4O_8$ (%): C, 35.57; H, 4.48; N, 13.83. Found: C, 35.68; H, 4.52; N, 13.65.

Suitable single crystals of **2** were obtained in a test tube via slow diffusion of a methanol solution containing H3isoani (0.2 mmol, 0.0276 g, 5 mL) over an aqueous interlayer, which separated the solutions at the top and bottom of the tube, and another aqueous solution containing $Co(NO_3)_2 \cdot 6H_2O$ (0.1 mmol, 0.0291 g, 5 mL).

3. Results and discussion

3.1. Description of the crystal structures

3.1.1. Structural description of {[Co(μ-3isoani)₂]·DMF}ₙ (**1**)

Compound **1** crystallises in the non-centrosymmetric orthorhombic *Pnn*2 space group as a racemic twin as indicated by Flack parameter (see crystallographic data, Table S9). The junction between cobalt (II) and 3isoani ligand under solvothermal conditions gives rise to an interpenetrated 3D open architecture, which contains voids occupied by DMF solvent molecules. The Co1 atom placed on the crystallographic binary axis exhibits a quite distorted environment established by the N_2O_4 donor set, which is best approach to an octahedral geometry as indicated by SHAPE programme ($S_{OC} = 3.63$) [41]. The high distortion of the environment is mainly caused by two of the oxygen atoms, which, belonging to the chelating carboxylate groups of two 3isoani ligands, are geometrically forced to bind to Co1 atom notably reducing the symmetry of the coordination shell. The coordination sphere is completed by the pyridyl nitrogen atoms pertaining to the other two 3isoani ligands, all of which renders a four connected node in the form of an adamantoid building unit (Fig. 1). Most relevant distances within the metal centres are summarised in Table 1.

As a result of the $\mu\text{-}\kappa N{:}\kappa^2 O,O'$ coordination mode of the organic ligand, the distance between metal centres along the bridge is relatively long (Co···Co distance is 8.796 Å). Considering the aforementioned building units as nodes and 3isoani ligands as linear linkers, the assembly of the building units forms a 3D diamond-like network as confirmed by TOPOS programme package
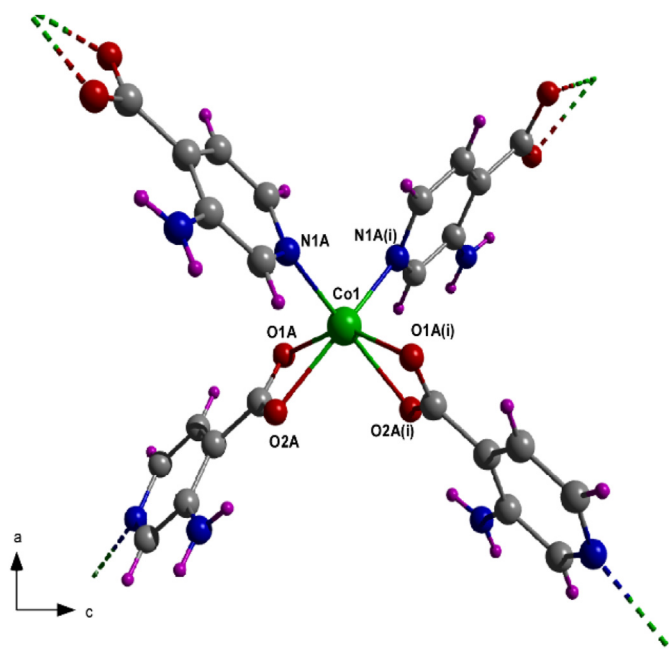
O. Pajuelo-Corral, S. Pérez-Yáñez, I.J. Vitorica-Yrezabal et al.

Materials Today Chemistry 24 (2022) 100794

Fig. 1. View of the adamantoid building unit of **1**. Colour coding: carbon (grey), hydrogen (pink), nitrogen (blue) and oxygen (red).

Table 1
Selected bond lengths for compound **1** (Å).

Co1−O1	2.078(2)	Co1−O2A (i)	2.233 (3)
Co1−O1A (i)	2.078 (2)	Co1−N1A	2.069 (3)
Co1−O2A	2.233 (3)	Co1−N1A (i)	2.069 (3)

[a] Symmetries: (i) −x+1, −y+1, z.

[42] (with **dia** topology and (6^6) point symbol). The resulting network leaves a huge volume that is occupied by a second equivalent subnetwork that crystallises in the catenated framework, which seems to stabilise the crystal building (Fig. S6). In fact, the interpenetrated frameworks are held together by the occurrence of N31A-H31B···O1A (ii) hydrogen bonds between carboxylate and −NH$_2$ moieties (Fig. S7 and Table S3). In addition, the amine groups establish a second hydrogen bond with the carboxylic oxygen atom of the same 3isoani ligand, a fact that endows the crystal building with a high thermal stability (see below). Despite the interpenetration, the framework still possesses a remarkable porosity (the geometrical porosity of **1** represents the 35.9% of the unit cell volume as indicated by PLATON) [43] arranged in the form of microchannels running along the crystallographic *b* axis (Fig. 2 and S8), which are occupied by disordered DMF solvent molecules. As shown in Fig. 2, the microchannels are characterised by narrow sections of *ca.* 3.7 Å joining the other regions of *ca.* 5.3 Å, which are the biggest cavities that are delimited by four aromatic rings of 3isoani ligands. Although the disordered guest molecule prevents a detailed study of the interaction with the framework, DMF molecules seem to establish a weak hydrogen bond with the amino group of the pyridine ring. It is worth mentioning that these compounds show close resemblance to the previously reported [Co(in)$_2$]$_n$ (where in = isonicotinato) [44], but for the fact that the ligand used in that work lacks the exocyclic amino group.

3.1.2. Structural description of [Co(3isoani)$_2$(H$_2$O)$_4$] (2)

Single-crystal X-ray analysis reveals that **2** crystallises in the *P*2$_1$/*c* space group in the form of monomeric complexes of formula [Co(3isoani)$_2$(H$_2$O)$_4$], which results from the assembly of Co(II) and
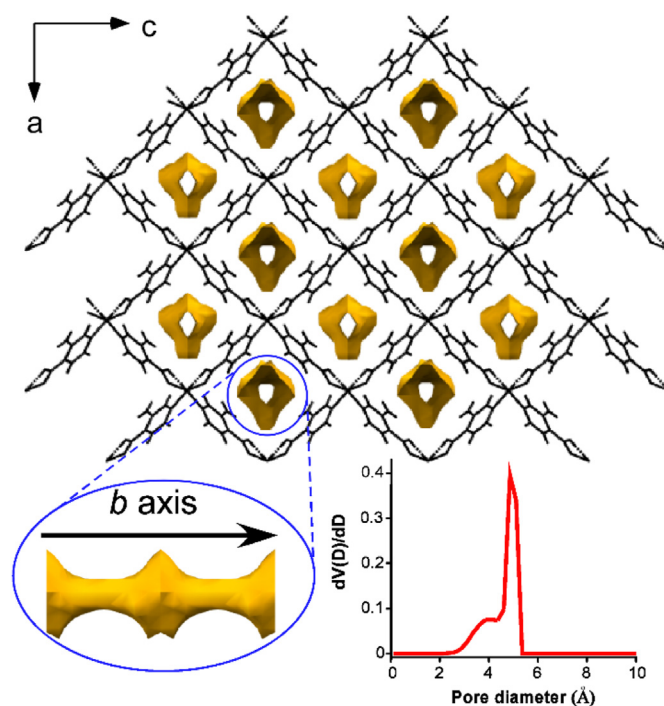

Fig. 2. Crystal packing of compound **1** showing the microchannels along the crystallographic *b* axis.

3isoani ions in aqueous media, a quite surprising fact, given that this compound is involved in a reversible structural transformation with the open 3D framework of **1** (see below). The metal centre is connected to four oxygen atoms of coordinated water molecules occupying the equatorial plane, whereas the main axis of the slightly distorted octahedral geometry (S$_{OC}$ = 0.107) contains two pyridyl nitrogen atoms of 3isoani ligands (Fig. 3).

Conversely to compound **1**, it is worth noticing that coordination distances are somewhat larger for Co−N (2.161 Å) than for Co−Ow
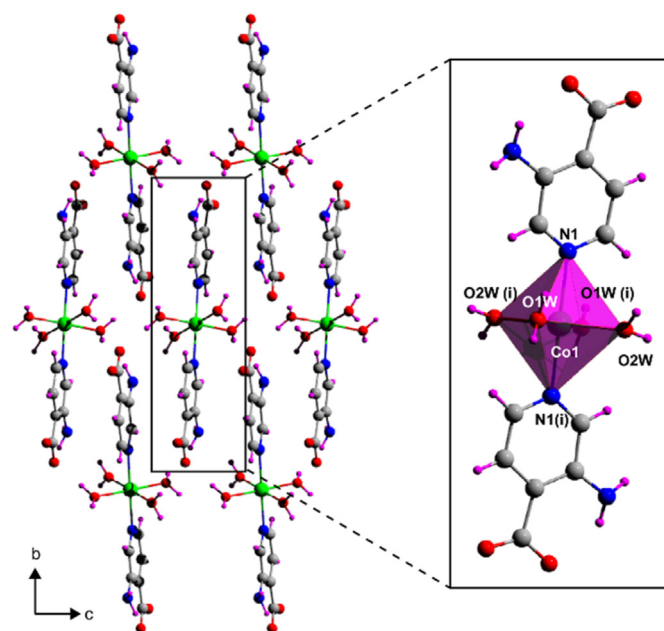

Fig. 3. Crystal packing of compound **2** with the monomeric complex highlighted.

(2.059−2.129 Å, see Table S4). Moreover, conversely to **1**, 3isoani ligand acts as a terminal ligand with the carboxylate groups remaining deprotonated and uncoordinated. As a consequence, these groups are involved in the hydrogen bonding network set out by the coordinated water molecules, which are able to successfully sustain the supramolecular crystal building, which is in turn further stabilised by the presence of π-π stacking interactions between the aromatic pyridine rings of neighbouring complexes (see Fig. S9 and Tables S5-S6).

3.2. Chemical stability tests: comments on structural transformations

The previously mentioned compounds are characterised for a drastic dynamic behaviour by being involved in a reversible structural transformation frame that allows the mutual interconversion between the three-dimensional and monomeric compounds (**1** ↔ **2**) in the presence of certain solvents. In this sense, when compound **1** is exposed to a prolonged humid environment (both to open atmosphere with high relative moisture or to aqueous medium), it rapidly captures water molecules that replace some of the ligand anions in the coordination shell of the 3D framework to completely reorganise the crystal structure and yield compound **2** (see ESI). This transformation also occurs in the opposite direction, and when the powdered sample of **2** is exposed to DMF (not only in solution but also in gas phase in a closed vessel), the monomeric complexes are able to reorganise by rebuilding the 3D backbone, whereas the coordinated water molecules are released from the metal centres and kept into the microchannels of compound **1**, making the process fully reversible (see Scheme 1). On another level, when single crystals of **1** are left to stand in the mother liquors, they undergo a slow single-crystal to single-crystal transformation to eventually yield a complex related to **2** in which two DMF lattice molecules are crystallised together with the monomeric complex, **2-DMF** hereafter (crystallographic data are reported in the ESI, see Table S9). Taking into account that the inclusion of the lattice solvent molecules in the structure does not promote significant changes in the coordination environment of Co(II) ion, the flexibility of the monomeric complex to adapt for distinct crystalline environments is an evidence to be emphasised. In fact, the soaking of **2-DMF** into DMF confirms the reversibility of the **1** ↔ **2-DMF** reaction, a process that occurs under the same conditions to the previously mentioned (**1** ↔ **2**) interconversion.

Structural transformations on exposure to different solvents are commonly observed in MOFs, although such a transformation from

Scheme 1. Summary of the reversible solvent-triggered **1** ↔ **2** transformations.
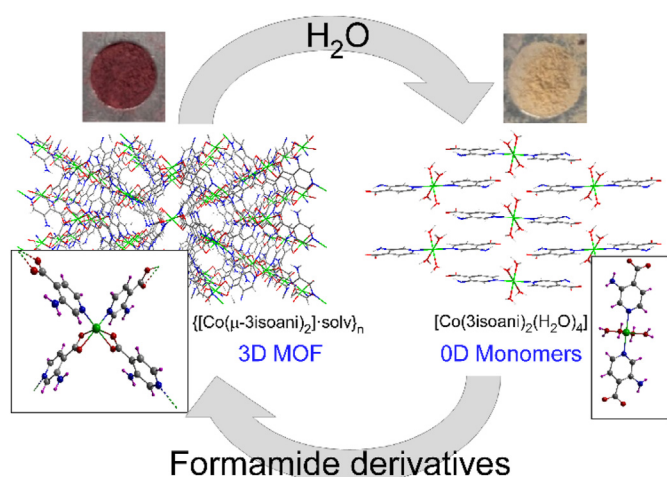
the zero-dimensional monomeric unity to a 3D open framework is not very common [45]. This drastic change is induced by the hydration/dehydration process taking place in the transformation. In fact, coordinated water molecules play a key role as they prevent the connection between nodes because (1) they act as terminal ligands and (2) they establish hydrogen bonds with the carboxylate groups of adjacent monomers, a fact that prevents the coordination of the carboxylic oxygen atoms to other metal centres to bridge them, preventing the growth of a structure of higher dimensionality. On another level, although there is no change in the coordination number, compounds **1** and **2** exhibit important differences in the coordination geometry (both of them may be described as octahedra although the coordination sphere is highly distorted in the case of **1**), a fact that can modulate the properties of the compounds as previously observed for other systems, for instance, in the field of photoluminescence and magnetism [46,47]. For starters, these geometrical differences involve important changes in the spectroscopic properties because absorption bands attributed to the Co-based ligand-field transitions are clearly more intense for **1** rather than **2** (Fig. S12), which could be due to a relaxation of the spectroscopic selection rules derived from the distorted environment of the former (discussed later on). Consequently, there is an obvious colour change of the material that can be traced by the naked eye, from reddish purple in **1** to a light brown colour in **2** (Fig. S13), a fact that may lead to the use of these materials as sensors for the potential detection of the solvents involved in the transformation (see further discussion hereinafter).

On another level, it must be highlighted that despite the high lability of compound **1** to react with water, it is very stable in other solvents (without the necessity of being completely dried, see S13 section of the ESI for further details), meaning that the transformations require a minimum of water to take place (as it is later discussed).

3.3. Thermal behaviour

To study the effect of the temperature on the crystal structure of **1**, thermodiffractometric and thermogravimetric measurements were performed over a polycrystalline sample. The recorded curve shows no mass loss until it releases its lattice DMF solvent molecules between 160°C and 270°C as confirmed by thermogravimetric/differntial temperature analysis (TG/DTA) (bringing a mass loss of 18.2% that is close to the theoretical loss of one DMF molecule). It is worth noticing that this process takes place at a higher temperature compared with free DMF boiling point, probably, as a consequence of the hydrogen bonding interactions established with the backbone of the MOF. A detailed thermodiffractometric study (Fig. 4) of the polycrystalline sample reveals that the main diffraction maxima are shifted to lower 2θ angles as the temperature increases, among which the most intense one shifts from 15.29° (RT) to 14.80° (250°C).

The drastic changes shown by the thermal evolution of the diffractograms only allowed performing Le Bail refinements by decreasing the symmetry of the space group, moving from the orthorhombic *Pnn*2 to the monoclinic *Pn*. In particular, the unit cell describes an expansion of 58% in its volume estimated from the pattern-matching refinements carried out on the diffractograms at different temperatures and whose parameters before and after the expansion are shown in Table S8, a fact that is in apparent contradiction with the expected volume contraction occurring during the solvent release. However, the observed evolution seems to be related with the large flexibility of the structure, probably derived from its interpenetrated nature, in such a way that subnetwork displacement occurring when lattice molecules are released rearranges the crystal building by placing the subnetworks

O. Pajuelo-Corral, S. Pérez-Yáñez, I.J. Vitorica-Yrezabal et al.
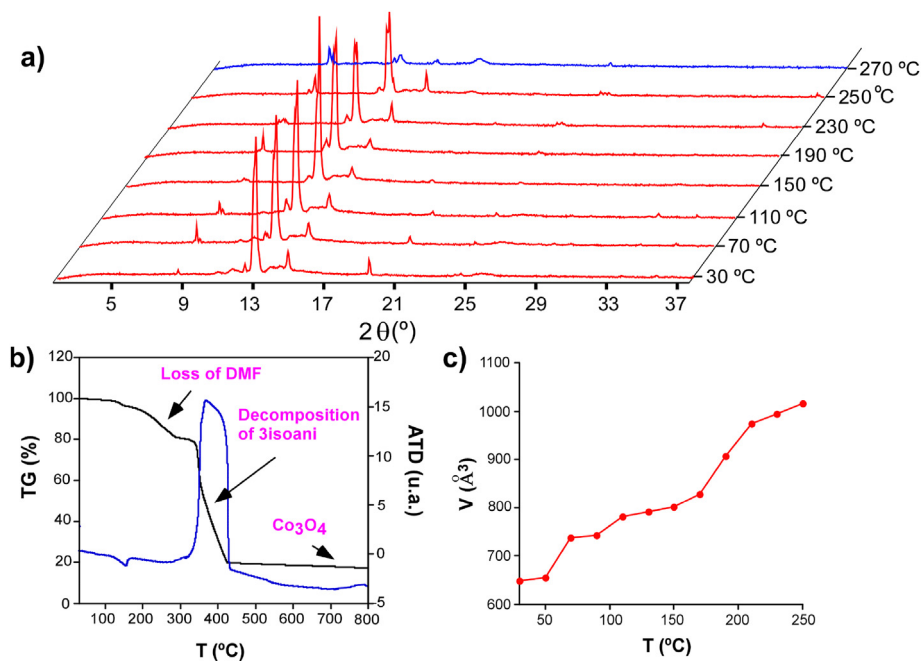
Materials Today Chemistry 24 (2022) 100794

Fig. 4. Analysis of the thermal behaviour of compound **1** showing (a) thermodiffractometry in the 30−270°C temperature range, (b) thermogravimetric plot and (c) evolution of cell volume with temperature.

farther apart from each other. Above 250°C, the diffraction pattern completely changes, showing some weak maxima at higher angles; however, because of the low diffraction capacity, it is not possible to guess any further structural detail. Finally, the decomposition of the organic part of the framework takes place between 360 and 410°C, giving rise to Co_3O_4 as a final residue.

3.4. Adsorption measurements on compound **1**

Motivated by the good thermal stability shown by the 3D open structure of compound **1**, to confirm its permanent porosity and gas uptake capacity, N_2 and CO_2 adsorption experiments were conducted on freshly prepared polycrystalline sample (taking no special care but for closing it on a hermetic container to avoid potential hydration and subsequent **1** → **2** transformation). To that end, the sample was outgassed at 150°C under vacuum for 6 h, showing a mass loss of *ca.* 18% (see ESI for further details), which, being so close to the experimental loss observed in the TG/DTA analysis, suggests the complete removal of DMF from the microchannels. Nevertheless, the first inspection by means of the N_2 adsorption measurement at 77 K revealed a residual uptake in the 0−1 bar range adsorption, with an isotherm showing higher adsorption in the high pressure range usually observed for the interparticle capillary condensation occurring for non-porous solids (see Fig. S14). Given that the activated MOF retains crystallinity and shows no obvious change in its structure as confirmed by PXRD, CO_2 isotherms were measured at higher temperatures to discard the possibility of a diffusion barrier derived from poor $N_2\cdots$framework interaction occurring because of narrow microchannels as previously described for other MOFs and supra-MOFs [48,49]. At 298 K, compound **1** presents an isotherm characterised by a rapid rise of the adsorbed volume of the gas followed by a progressive increase up to 3.35 mmol/g, a value that seems to practically reach a plateau at 1 bar. Taking into account the formula weight of the activated framework, this uptake corresponds to 0.90 molecules of CO_2 per Co(II) ion, that is, {[Co(μ-3isoani)$_2$]·0.90 CO_2}$_n$ (Fig. 5).

As expected, when the temperature of the experiment is dropped to 273 K, the MOF shows a stronger capture of CO_2 at low pressure as inferred from its steeper increase in the isotherm, which in turn reaches a value of 4.09 mmol/g (1.36 CO_2 molecules per formula). Note that the desorption curves are almost superimposed to the adsorption branches signifying that the gas diffuses slowly but does not get stuck in spite of the narrowness of the microchannels, which confirms the flexible nature of the framework. It is also worth noticing that this MOF qualifies in the upper intermediate adsorbents in terms of gravimetric capacity because 14.5% and 18.0% of CO_2 captured (g/g) outperforms the results obtained for other well-known MOFs, such as MIL-53(Al, Cr), MOF-5, MOF-177 or even most of ZIF materials in their bulk state [50,51]. Motivated by the steep slope shown in the low coverage regime of the isotherms, adsorption enthalpies (Q_{st}) were calculated by fitting the curves at both temperatures to the modified Clausius−Clapeyron equation, for which the third isotherm at 283 K was additionally measured (see ESI) [52]. As observed in Fig. S17, the value of Q_{st} may be considered as nearly constant during the loading range (of *ca.* 26 kJ/mol and plotting a positive slope with increasing CO_2 loading) although a slight increasing trend is observed. This behaviour is not common but has been already observed for other MOFs in which favourable adsorbate−adsorbate interactions occur at high loadings, as it is the case of NKMOF-8-Br, MUF-15, ZIF-7 and NUP-1 MOFs [53−56]. Coming back to the structure of **1**, such interactions are possibly motivated by the quite regular tubular microchannels delimited by the aromatic rings of the ligands, in which guest CO_2 molecules would join one another to preferably interact with the framework. However, to have a better understanding of the Q_{st} vs. CO_2 loading trend as well as the interactions involving the CO_2 molecules in the framework, we decided to perform the *in situ* structural determination of the gas adsorbed at variable pressures and temperatures using single-crystal X-ray diffraction (XRD; see the crystallographic data in Tables S10-S11in the ESI). On activation of a single-crystal by heating at a temperature of 230°C, no residual electron density was observed within the pores, indicating the successful evacuation of DMF molecules. By applying
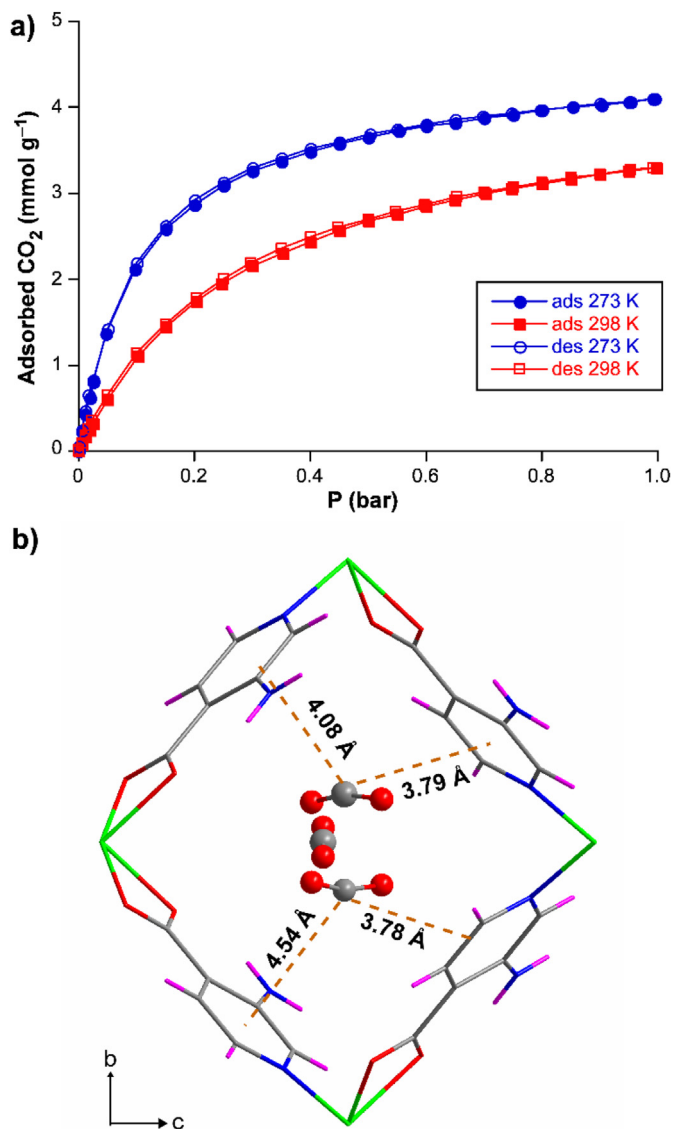
Fig. 5. (a) Adsorption and desorption isotherms of compound **1** recorded at 298 and 273 K. (b) Crystal structure of **CO_2@1** at 298 K and 1 bar showing the interactions between guest molecules and the framework.

1 bar of CO_2 at 298 K, electron density observed in the voids allowed the refinement of three disordered CO_2 molecules per asymmetric unit (applying rigid bodies) that account for a total crystallographic occupancy of 0.77 molecules per formula unit (**CO_2@1** hereafter). This amount is slightly lower than that estimated from the isotherms, which may be attributed to the disorder occurring for these molecules that penalises their diffraction and prevents a complete assignation of the electron density. As illustrated in Fig. 5b, two of the molecules are able to maximise their interaction with two adjacent rings of 3isoani ligands (showing distances between the centroid of the rings and CO_2 in the range of 3.78–4.60 Å), whereas the third gas molecule represents a disordered situation of the latter two molecules staying farther from the ligands. The disordered entrance of CO_2 in the microchannels seems to support the previous hypothesis raised about the cause of the increasing trend of the isosteric heat. Moreover, this scenario is quite enlightening because it discards the amino group (-NH_2) pending from the subnetwork as a potential interaction site despite the fact that these Lewis bases are known to interact strongly with the acidic CO_2 molecules,

thereby enhancing the adsorption of CO_2 molecules [57−60]. Probably, this is a consequence of the intra- and inter-molecular hydrogen bonds established by the amino groups, as discussed in the structural description section, which prevent significant interactions with the guest molecules, in such a way that the closest C=O⋯N distance is of *ca.* 3.55 Å. On increasing the pressure, no significant change of the interaction scheme of guest molecules is observed, while there is an increase in the occupancy of CO_2 molecules up to 1, 1.2 and 1.3 per formula at 2.5, 5 and 10 bars of pressure, respectively; meaning that the maximum uptake observed in the adsorption isotherm (1 bar, 298 K) is indeed close to the value at saturation. Remarkably, the experiment does not seem to force the rearrangement of the interpenetrated framework (for instance, through a subnetwork displacement) as potentially occurring for interpenetrated MOFs because the unit cell parameters remain remarkably unchanged [61]. The latter is also supported by the slight increase in the gas uptake on increasing the pressure.

To finish up with the structural study of **CO_2@1**, diffraction data were acquired on a single crystal by slowly dropping the temperature and keeping the pressure at 10 bar. As expected, the decrease in temperature significantly enhances the gas uptake capacity of the material, leading to the adsorption of 2.4 molecules of CO_2 per formula at a temperature of 225 K, in which the occupancy of the molecules rises but the guest⋯framework interactions are kept unaltered. With this in mind, the disordered and progressive occupation of the CO_2 molecules adsorbed in the voids of the MOF could perfectly explain the aforementioned trend for the Q_{st} as the CO_2 loading is increased. All these experiments confirm the good CO_2 adsorption capacity of this MOF despite its low chemical stability in water, a fact that may limit its application as adsorbent while it, nonetheless, opens the way to an interesting sensing capacity (see sections below).

3.5. Magnetic measurements

3.5.1. Static magnetic properties

Variable temperature (2−300 K) dependence of the magnetic susceptibility data was analysed over polycrystalline samples of compounds **1** and **2** under a *dc* applied field of 1,000 Oe. Both compounds present a similar behaviour as shown in Fig. 6. At room temperature, compounds **1** and **2** show $\chi_M T$ products of 3.07 and 2.80 cm^3 K mol^{-1} per Co(II) atom, which are significantly higher than the expected value for an octahedral Co(II) ion spin-only value (1.87 cm^3 K/mol with $g = 2.01$), suggesting the presence of certain spin-orbit coupling (SOC). On cooling, the $\chi_M T$ values remain somewhat constant up to 100 K, below where the curves drop more abruptly off to a value of 1.89 and 1.78 cm^3 K/mol at 2 K, respectively, for **1** and **2**. The latter may be attributed to the first-order SOC effect usually present in highly distorted Co(II)-based polyhedron, although the contribution of weak antiferromagnetic interactions may not be discarded. The χ_M^{-1} vs. T curve follows the Curie-Weiss law in both compounds (Figs. S18 and S22) in the 50−300 K temperature range with $C = 2.87$ and 0.54 cm^3 K/mol and $\theta = -0.30$ and -0.19 K, which confirms the absence of significant antiferromagnetic interactions among metal centres, in good agreement with the long distance imposed among spin carriers in both structures. In any case, the absence of exchange interaction through the bridging ligands in 1 is further discarded by means of DFT-computed broken symmetry procedure on a dimeric model, which gives a negligible exchange value ($J = -0.02$ cm^{-1}, Fig. S25). In view of the six-connected CoN$_2$O$_4$ environments present in both compounds, magnetic susceptibility curves were fitted using PHI programme [62] with the Hamiltonian given in eq. (1) [63] to analyse the SOC effect:
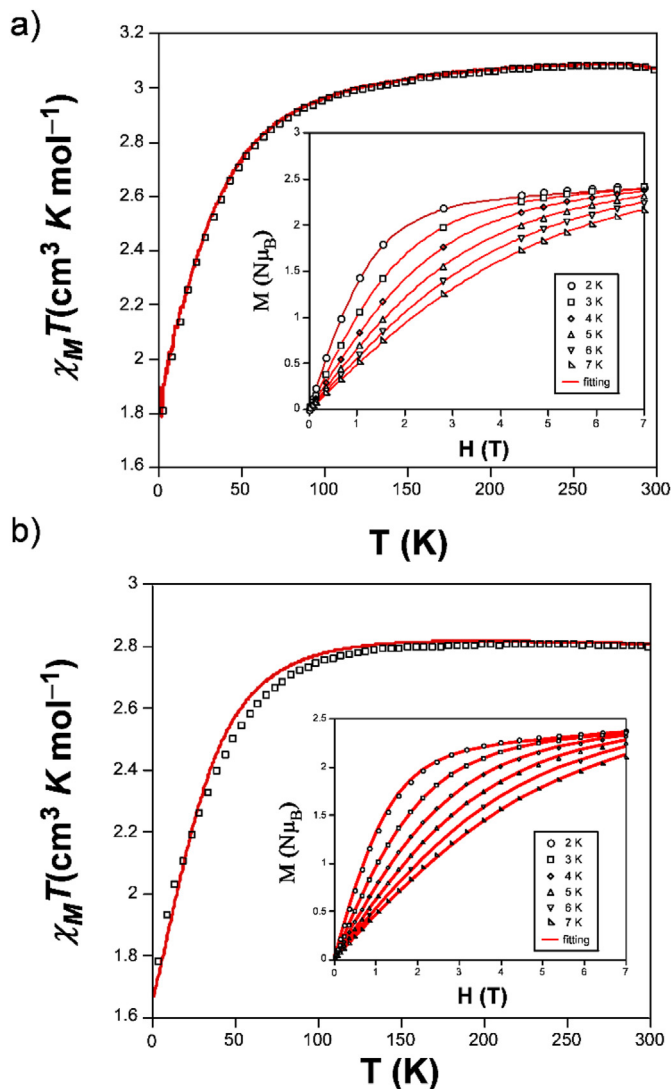
O. Pajuelo-Corral, S. Pérez-Yáñez, I.J. Vitorica-Yrezabal et al.

Materials Today Chemistry 24 (2022) 100794

Fig. 6. Simultaneous fitting of $\chi_M T$ vs. T and M vs. H plots according to eq. (2) for (a) **1** and (b) **2**.

$$\hat{H} = \sigma\lambda(L_{Co}S_{Co}) + \Delta\left[L_{z,Co}{}^2 - L_{Co}(L_{Co} + 1/3)\right] + \mu_B H(-\sigma L_{Co} + gS_{Co})$$

(1)

where all parameters have their usual meaning. The following results give a quite well fitting of the data (see Figs. S19 and S23 for **1** and **2**, respectively): $\lambda = -117$ cm^{-1}, $\Delta = 390$ cm^{-1}, $\sigma = -1.10$ and $g = 2.21$ with R $= 4.3 \times 10^{-2}$ for **1** and $\lambda = -194$ cm^{-1}, $\Delta = 370$ cm^{-1}, $\sigma = -0.49$ and $g = 2.32$ with R $= 1.3 \times 10^{-2}$ for **2**.

In view of the large Δ value, it may be assumed that only the two lowest Kramers doublets of the $^4A_2$ ground state are thermally populated, meaning that the energy gap separating them from the excited lowest-lying ones corresponds to the axial *zfs* within the quartet state. This is further confirmed by the magnetisation curves collected in the 0−7 T magnetic field and 2−7 K temperature range do not reach the theoretical saturation for $S = 3/2$ ($M_{sat} = 3.3$, with $g = 2.2$). Moreover, the reduced magnetisation curves do not superimpose with each other in a single master curve (see ESI, Figs. S21 and S24 for **1** and **2**, respectively), which points to the presence of substantial magnetic anisotropy. Accordingly, the

magnetic properties may be interpreted by the spin Hamiltonian of eq. (2):

$$\hat{H} = D\left(\hat{S}_z^2 - \hat{S}/3\right) + E\left(\hat{S}_x^2 + \hat{S}_y^2\right) + \mu_B H g \hat{S}$$

(2)

where *S* is the spin ground state ($S = 3/2$), *D* and *E* correspond to the axial and rhombic magnetic anisotropies, respectively, and *H* is the applied magnetic field. Best fitting using both (susceptibility and magnetisation) data by PHI programme gives $D = -57.9$ cm^{-1}, $E < -0.1$ and $g = 2.2$ with R $= 2.8 \times 10^{-2}$ for **1**, in line with reported octahedral Co(II)-based coordination polymers (CPs) [64,65]. The set of data for **2**: $D = +76.3$ cm^{-1}, $E/D = 0.13$ and $g = 2.4$ with R $= 2.1 \times 10^{-2}$, indicates an easy-plane magnetic anisotropy with a non-negligible contribution of transverse anisotropy, a fact that has been commonly observed in slightly distorted Co(II) octahedral compounds [66,67]. Moreover, as a consequence of such positive sign, the $m_s = \pm1/2$ doublet is below the $m_s = \pm3/2$ doublet.

To further corroborate the magnetic properties of these compounds, we decided to compute *ab initio* calculations using the ORCA suit programme [68] on both the X-ray crystal structures and optimised models to discard any possible effect regarding the sign and magnitude of the magnetic anisotropy derived from small structural distortions [69]. To our surprise, the computed values on the XRD model of **1** notably differ from the experimental ones assuming an octahedral geometry (Table 2), even for the sign of the parameter (since the computed *D* presents a positive value in contrast to the experimental negative one). Moreover, the splitting of the d orbitals of Co(II) obtained by CASSCF/NEVPT2 calculations is concordant with a distorted tetrahedral geometry rather than an octahedral one because e_g molecular orbitals lie below t_{2g} molecular orbitals (Fig. 7). In fact, the computed dominant ground-state electronic arrangement was found to be $(d_z^2)^2(d_{x-y}^2)^2(d_{yz})^1(d_{xz})^1(d_{xy})^1$ with 71% of contribution. This result, though somewhat unexpected, can be well explained on the basis of the coordination arrangement adopted by 3isoani ligands. Coming back to the structural description, the framework consists of diamond-like (4-connected) topological nodes, in which the chromophore indeed possesses four main coordination bonds (N$_2$O$_2$ set with *ca.* 2.07 Å) and other two weaker bonds (chelating O atoms at *ca.* 2.23 Å), meaning that the geometry of **1** could also be referred to as distorted tetrahedron. It is worth highlighting that similar findings have been already reported for other related CPs built from CoN$_2$(CO$_2$)$_2$ environments [37,70]. Therefore, fitting of the experimental susceptibility and magnetisation data were repeated by considering a tetrahedral geometry from which the following set of parameters were obtained with the Hamiltonian of eq. (2): $D = +38.9$ cm^{-1}, $E/D = 0.16$ and $g = 2.56$ with R $= 2.1 \times 10^{-3}$ (Fig. S20). As observed, the latter assumption not only improves the fitting but also estimates values that are closer to the computed results (showing similar deviations to other works) [67,71], confirming that a distorted tetrahedral environment provides a reliable description of the magnetic properties. A detailed analysis of the anisotropy of **1** indicates that excited states contributing (the first

Table 2

Results from NEVPT2 calculations on the XRD structures showing the main parameters for compounds **1** and **2**.

Compound	**1**	**2**
D (DKD$_{1-2}$, DKD$_{1-3}$)^a cm^{-1}	+53.6 (+27.7, +26.4)	+81.1 (+46.4, +25.9)
E/D	0.10	0.25
g_{xx}, g_{yy}, g_{zz}	2.11, 2.51, 2.62	2.00, 2.42, 2.87
g_{iso}	2.42	2.43
ΔE (1−2), ΔE (1−3)	1374.3, 1702.3	934.1, 1089.1

^{a} The two values in the parentheses after D represents the contribution to D from the ground to first and ground to second excited state transitions, respectively.
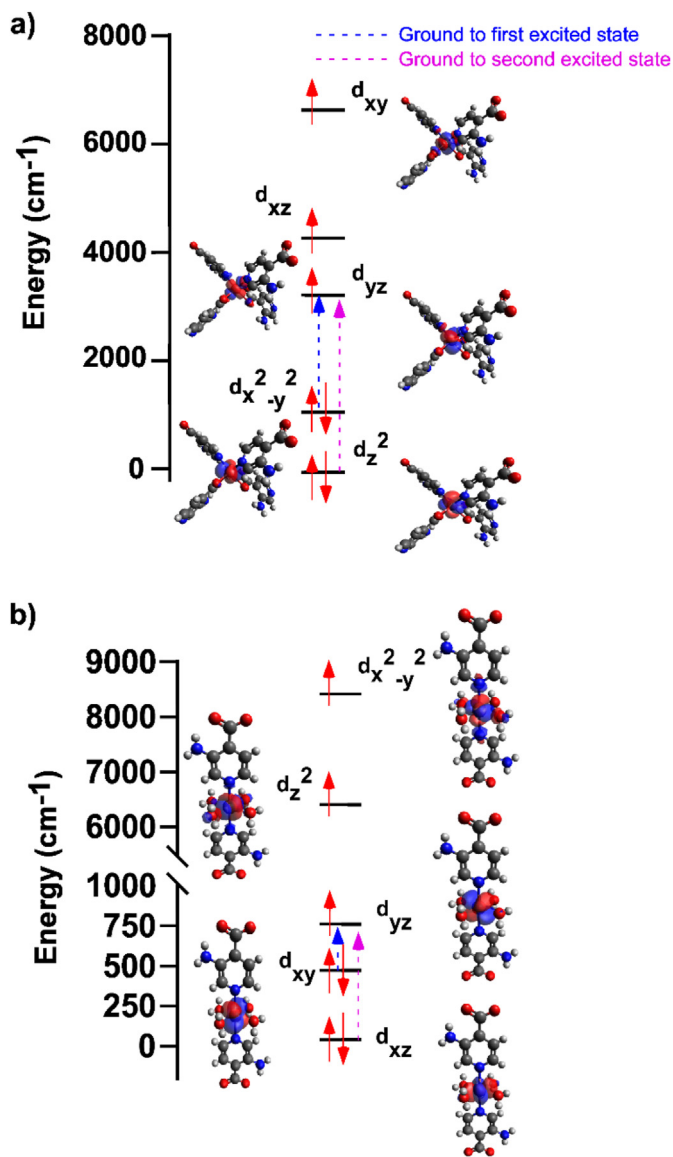
O. Pajuelo-Corral, S. Pérez-Yáñez, I.J. Vitorica-Yrezabal et al.

Materials Today Chemistry 24 (2022) 100794

Fig. 7. NEVPT2 computed d-orbital splitting for compounds (a) **1** and (b) **2**. Brick lines represent dominant electronic transitions from ground to first and ground to second excited states, respectively.

and second states as inferred from their transition energies, see Table 2) are also multideterminant in nature with $(d_z^2)^2(d_{x-y}^{22})^1$ $(d_{yz})^2(d_{xz})^1(d_{xy})^1$ and $(d_z^2)^1(d_{x-y}^{22})^2(d_{yz})^2(d_{xz})^1(d_{xy})^1$ as the dominant electronic arrangements for first and second excited states with a contribution 54% and 49%, respectively. Consequently, the largest two contributions to *D* parameter arise from $d_{x-y}^{22} \rightarrow d_{yz}$ and $d_z^2 \rightarrow d_{yz}$ transitions from ground to first and ground to second excited states, respectively.

On its part, the computed values (Table 2) for **2** support the easy-plane anisotropy of the paramagnetic centre. The electronic ground state indicates the following arrangement: $(d_{xz})^2(d_{xy})^2(d_{yz})^1(d_z^2)^1(d_{x-y}^{22})^1$ with 91% of contribution, which satisfies the expected orbital splitting of a weakly distorted octahedron. The first and second excited states, with $(d_{xz})^2(d_{xy})^1(d_{yz})^2(d_z^2)^1(d_{x-y}^{22})^1$ (55% of weight) and $(d_{xz})^1(d_{xy})^2(d_{yz})^2(d_z^2)^1(d_{x-y}^{22})^1$ (52% of weight) arrangements, indicate that the main contributions to anisotropy arise from the ground to the first state $d_{xy} \rightarrow d_{yz}$ and ground to second excited state $d_{xz} \rightarrow d_{yz}$ transitions. Note that both transitions do not contribute equally to the *D* parameter, but the contribution of the

former is significantly larger according to its smaller energy gap [72,73].

Generally speaking, considering both compounds, it must be noticed that the computed results overestimate the experimental values of most of the parameters, as pointed out by some authors [74]. A comparison of the theoretical results performed over the distinct models (XRD structure, H-optimised and fully optimised models) does not reveal any systematic trend, meaning that the increase/decrease of the magnetic anisotropy parameters (see Tables S12 and S13) is caused by the change of multiple geometrical factors affecting the coordination sphere.

3.5.2. Dynamic magnetic properties

To study the SMM behaviour, alternating current (*ac*) magnetic susceptibility measurements were performed over polycrystalline samples of **1** and **2** at low temperature. In the absence of an external magnetic field, no out-of-phase (χ_M') signals were observed, probably because of a fast relaxation due to the quantum tunnelling of the magnetisation effect (QTM). The application of an external magnetic field of 1,000 Oe leads to some frequency-dependent maxima for compounds **1** and **2**, suggesting the suppression of the QTM phenomenon (Fig. 8).

In the temperature-dependent *ac* plots, compound **1** presents a nice set of maxima showing the maxima at the highest frequency (10,000 Hz) at 4.8 K. The maxima are comparatively wider and shifted to higher temperatures for **2**, with the χ_M' signal of 10,000 Hz peaking at 7.6 K. Accordingly, Cole-Cole plots were generated in the 2.0−5.2 and 2.0−7.6 K ranges for **1** and **2** (Fig. S27). The semicircular-shaped curves, fitted with the generalized Debye model, showed α values in the range of 0.30−0.08 and 0.20−0.02 for compounds **1** and **2**, respectively, which suggests the presence of more than one relaxation pathway, especially at low temperatures. In fact, the plot of the data according to the Arrhenius law (Eq. (3)) in the Ln(τ) vs. 1/T form adopts a curvilinear shape that only retains linearity in the high-temperature region. Fitting of the data in the high temperature range gives energy barriers for the reversal of the magnetisation (U_{eff}) of 15.4 K and 45.6 K with τ_0 of 8.63×10^{-7} s and 4.68×10^{-8} s for **1** and **2**, respectively; values that are concordant with other reported Co(II)-based magnets [75].

$$\tau = \tau_0 \exp\left(U_{eff} \big/ \kappa_B T\right) \quad (3)$$

However, these values for the energy barrier are far from those expected for the Orbach process according to the gap for the reversal of the magnetisation ($\Delta U_{eff} \approx 2D$ when $E = 0$ and $\Delta U_{eff} \approx 2\sqrt{D^2 + 3E^2}$ when $E \neq 0$) [76]. Taking into account that no real levels exist below ≈ 120 cm^{-1} and 150 cm^{-1} (taking into account the experimental values of *D* and *E*) for **1** and **2**, respectively, other processes rather than Orbach process are more likely to be involved in the magnetic relaxation. Accordingly, the data could be fitted to the simultaneous presence of Raman and QTM for **1** (Eq. (4)) and Direct and Raman for **2** (Eq. (5)), giving the following set of parameters: $\tau_{QTM} = 4.90 \times 10^{-4}$ s, $B_{raman} = 153.9$ s^{-1} K^{-n} with n = 3.6 for **1** and $A_{direct} = 1,183$ s^{-1} K^{-1}, $B_{raman} = 0.88$ s^{-1} K^{-n} with n = 5.0 for **2** (see Fig. 8). Although a n = 9 value is expected for Kramers ions in Raman involved relaxation processes, smaller n values in the range of 1−6 can be considered as reasonable and usually observed for Co(II)-based CPs [67,77,78].

$$\tau^{-1} = \tau_{QTM}^{-1} + B_{Raman}T^n \quad (4)$$

$$\tau^{-1} = A_{direct}T + B_{Raman}T^n \quad (5)$$

In any case, irrespective of the values obtained in the fitting,

O. Pajuelo-Corral, S. Pérez-Yáñez, I.J. Vitorica-Yrezabal et al.
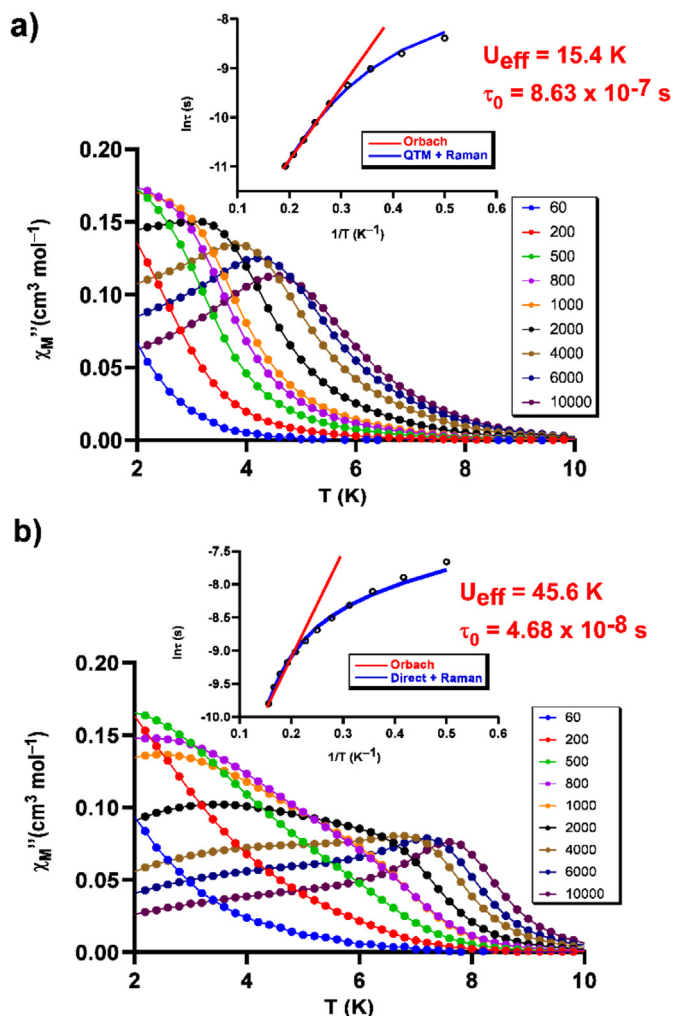
Materials Today Chemistry 24 (2022) 100794

Fig. 8. Temperature dependence of the χ_M'' signals for compounds (a) **1** and (b) **2** under an applied field of 1,000 Oe showing the temperature dependence for the relaxation times and best fits of the data to different relaxation processes.

much more significant is the overall change in the magnet behaviour occurring between compounds **1** and **2**. In addition to the field-induced different SMM behaviour, activated at higher temperatures for **2**, the mechanisms involved in the relaxation processes are also different. Taking into account that this behaviour is linked to an evident colour change shown by the sample during the **1** ↔ **2** transformation, these findings make one think about the potential use of Co/3isoani system as a colourimetric sensor to detect drastic changes of solvents in liquid media.

3.6. Solvent sensing activity by Co/3isoani

To determine the selectivity of the sensing capacity and, thereby, the scope of the potential applicability of this system, we immersed compound **2** in additional solvents with a similar nature to DMF. Specifically, polycrystalline samples of **2** were immersed in formamide (Form), DEF (N,N-diethylformamide) and DMA (N,N-dimethylacetamide). These solvents were selected by their similarity to DMF, assuming that they will reproduce a similar hydrogen bonding pattern with the framework. In all cases, as well as in DMF, we noticed a colour change of the powder from slight brown to reddish purple (Fig. S30), in addition to a change in the PXRD pattern (Fig. S31), indicative of the completion of **2** → **1**

transformation. This leads to the crystallisation of compounds **1-Form**, **1-DEF** and **1-DMA** with equivalent formulae to the isoreticular compound **1** (**1-DMF**), suggesting that they all exert a kind of templating effect that helps in the crystallisation of the 3D framework. It must be noted that in the case of formamide, the transformation reverts back to compound **2** as soon as the powder is taken out from the solvent so fast that a diffractogram of **1-Form** could not be obtained. In fact, the speed of the transformation seems to be dictated by the size of the solvent molecule as earlier reported by other authors [79] because the smallest Form induces an instantaneous conversion, whereas the biggest DEF requires a minimum of 24 h. Further studies were also carried out by immersing samples of **2** in other typical solvents of different chemical nature (i.e. containing distinct chemical functions), such as methanol, ethanol, acetonitrile and acetone, showing no colour change.

To get deeper insights into these related transformations and evaluate the versatility of the system, synthetic conditions to obtain **1** were reproduced by replacing DMF with DEF, in such a way that single crystals of **1-DEF** were obtained. The X-ray crystal structure (see crystallographic data, Table S9) confirms the isoreticular nature of the compound that possesses DEF molecules crystallised in the microchannels instead of DMF present in the original compound. Therefore, we can assume that the rest of solvents (Form and DMA) are able to template the **2** → **1** transformation, given that upon the immersion of **2** in the solvents produces purple-coloured samples.

4. Conclusions

In this work, we present a very versatile system consisting of two Co-based compounds with 3-aminoisonicotinato (3isoani) ligand, which crystallise in the form of two interchangeable solvent-induced structures: 3D MOF (compound **1**) or monomer-based supramolecular architecture (compound **2**). The MOF is built from topologically pseudo-tetrahedral $[CoN_2(CO_2)_2]$ units characterised for a largely distorted environment, which are linked one another into a two-fold interpenetrated diamond-like framework that contains tubular microchannels occupied by DMF with pore apertures of 5.3 Å at the most. The 3D MOF possesses somewhat low chemical stability because its exposure to open atmosphere (capturing water from moisture) triggers a spontaneous structural transformation that leads to the monomer-based compound **2**, which features a low distorted octahedral $[CoN_2(H_2O)_4]$ metal environment. Interestingly, the **1** → **2** transformation reverts back to the 3D framework by exposing the solid sample to vapours of DMF (or related formamide derivatives) or by immersing it in the solvent because these solvents play a kind of templating effect in the recrystallisation.

In spite of the limited chemical stability of compound **1** when exposed to water or moisture, its high thermal stability (it remains crystalline up to 250°C) allows yielding a permanently porous material under dry conditions. Accordingly, the MOF shows a negligible N_2 adsorption capacity but a very high capacity to capture CO_2 at room temperature of 3.35 mmol/g, which corresponds to an uptake of 0.90 molecules of the gas per formula unit (and cobalt ion). These results are in line with XRD experiments on a single crystal during *in situ* CO_2 adsorption measurements, which reveal an occupancy of 0.77 disordered CO_2 molecules that mainly interact with aromatic rings of 3isoani ligands.

Experimental magnetic measurements and CASSCF/NEVPT2 calculations reveal that both cobalt (II) compounds present field-induced SMM behaviour at low temperature derived from easy-plane magnetic anisotropy with considerable SOC, although the magnetic relaxation processes involved differ as a consequence of

their distinct coordination environment. On the one hand, the orbital splitting in **1** is best described as a distorted tetrahedral $CoN_2(CO_2)_2$ environment, given the large distance of Co−O bonds involved in the chelate rings. In this case, the SOC mainly arises from $d_{x^2-y^2} \rightarrow d_{yz}$ and $d_{z^2}^2 \rightarrow d_{yz}$ transitions and the slow magnetic relaxation proceeds through Raman and QTM mechanisms. On the other hand, the slightly distorted octahedral environment of **2** gives rise to the increase of zfs parameters arising from ground to first $d_{xy} \rightarrow d_{yz}$ and ground to second excited state $d_{xz} \rightarrow d_{yz}$ transitions, making the magnetic relaxation to proceed at a higher temperature by means of Raman and direct mechanisms.

Interestingly, in addition to their magnetic properties, these two crystalline compounds also differ in their colour since compound **1** is deep purple, whereas **2** is light brown. Further studies to explore the **1** ↔ **2** transformation with related solvents (formamide, N,N-dimethylacetamide and N,N-diethylformamide) show the same results with variable transformation rates according to the size of the molecule. These results are in agreement with the fact that solvent molecules must occupy the microchannels to template the growth of the 3D framework of **1**, whereas the contact with H_2O turns the latter into compound **2** in all cases. All in all, the exciting colour change together with reversibility between the two interchangeable compounds, make this system a really promising platform to develop materials with high potential sensing H_2O and/or amide-based solvent derivatives.

Author contributions

O.P.-C. contributed to investigation, data curation and writing the original draft. S.P.-Y. contributed to reviewing and editing the article and resources. I.J.V.-Y. contributed to investigation and formal analysis. G.B. contributed to validation, formal analysis and investigation. A.Z.-L. contributed to investigation and formal analysis. A.R.-D. contributed to resources and data curation. J.M.S. contributed to funding acquisition, supervision and visualisation. J.C. contributed to validation, methodology, conceptualisation, writing the original draft, data curation and project administration.

Declaration of competing interest

The authors declare that they have no known competing financial interests or personal relationships that could have appeared to influence the work reported in this paper.

Acknowledgements

Appendix A. Supplementary data

Supplementary data to this article can be found online at https://doi.org/10.1016/j.mtchem.2022.100794.

References

[1] L. Jiao, J.Y.R. Seow, W.S. Skinner, Z.U. Wang, H.-L. Jiang, Metal−organic frameworks: structures and functional applications, Mater. Today 27 (2019) 43−68, https://doi.org/10.1016/j.mattod.2018.10.038.

[2] J.R. Li, J. Sculley, H.C. Zhou, Metal-organic frameworks for separations, Chem. Rev. 112 (2012) 869−932, https://doi.org/10.1021/cr200190s.

[3] H. Li, K. Wang, Y. Sun, C.T. Lollar, J. Li, H.C. Zhou, Recent advances in gas storage and separation using metal−organic frameworks, Mater. Today 21 (2018) 108−121, https://doi.org/10.1016/j.mattod.2017.07.006.

[4] J. Liu, L. Chen, H. Cui, J. Zhang, L. Zhang, C.Y. Su, Applications of metal-organic frameworks in heterogeneous supramolecular catalysis, Chem. Soc. Rev. 43 (2014) 6011−6061, https://doi.org/10.1039/c4cs00094c.

[5] J. Cepeda, M. Pérez-Mendoza, A.J. Calahorro, N. Casati, J.M. Seco, M. Aragones-Anglada, P.Z. Moghadam, D. Fairen-Jimenez, A. Rodríguez-Diéguez, Modulation of pore shape and adsorption selectivity by ligand functionalization in a series of "rob"-like flexible metal-organic frameworks, J. Mater. Chem. A. 6 (2018) 17409−17416, https://doi.org/10.1039/c8ta04316g.

[6] D. Yang, B.C. Gates, Catalysis by metal organic frameworks: perspective and suggestions for future research, ACS Catal. 9 (2019) 1779−1798, https://doi.org/10.1021/acscatal.8b04515.

[7] H. Li, L. Li, R.-B. Lin, W. Zhou, Z. Zhang, S. Xiang, B. Chen, Porous metal-organic frameworks for gas storage and separation: status and challenges, EnergyChem 1 (2019) 100006, https://doi.org/10.1016/j.enchem.2019.100006.

[8] O.M. Yaghi, M. O'Keeffe, N.W. Ockwig, H.K. Chae, M. Eddaoudi, J. Kim, Reticular synthesis and the design of new materials, Nature 423 (2003) 705−714, https://doi.org/10.1038/nature01650.

[9] O.K. Farha, I. Eryazici, N.C. Jeong, B.G. Hauser, C.E. Wilmer, A.A. Sarjeant, R.Q. Snurr, S.T. Nguyen, A.Ö. Yazaydin, J.T. Hupp, Metal-organic framework materials with ultrahigh surface areas: is the sky the limit? J. Am. Chem. Soc. 134 (2012) 15016−15021, https://doi.org/10.1021/ja3055639.

[10] L. Feng, K.Y. Wang, X.L. Lv, T.H. Yan, H.C. Zhou, Hierarchically porous metal-organic frameworks: synthetic strategies and applications, Natl. Sci. Rev. 7 (2020) 1743−1758, https://doi.org/10.1093/nsr/nwz170.

[11] X. Liu, L. Zhang, J. Wang, Design strategies for MOF-derived porous functional materials: preserving surfaces and nurturing pores, J. Mater. 7 (2021) 440−459, https://doi.org/10.1016/j.jmat.2020.10.008.

[12] G.R. Desiraju, Crystal engineering: solid state supramolecular synthesis, Curr. Opin. Solid State Mater. Sci. 2 (1997) 451−454, https://doi.org/10.1016/S1359-0286(97)80088-5.

[13] V. Guillerm, D. Kim, J.F. Eubank, R. Luebke, X. Liu, K. Adil, M.S. Lah, M. Eddaoudi, A supermolecular building approach for the design and construction of metal-organic frameworks, Chem. Soc. Rev. 43 (2014) 6141−6172, https://doi.org/10.1039/c4cs00135d.

[14] M. Eddaoudi, D.F. Sava, J.F. Eubank, K. Adil, V. Guillerm, Zeolite-like metal-organic frameworks (ZMOFs): design, synthesis, and properties, Chem. Soc. Rev. 44 (2015) 228−249, https://doi.org/10.1039/c4cs00230j.

[15] M. Zhang, M. Bosch, T. Gentle, H.C. Zhou, Rational design of metal-organic frameworks with anticipated porosities and functionalities, CrystEngComm 16 (2014) 4069−4083, https://doi.org/10.1039/c4ce00321g.

[16] H.L. Jiang, T.A. Makal, H.C. Zhou, Interpenetration control in metal-organic frameworks for functional applications, Coord. Chem. Rev. 257 (2013) 2232−2249, https://doi.org/10.1016/j.ccr.2013.03.017.

[17] Y.-N. Gong, D.-C. Zhong, T.-B. Lu, Interpenetrating metal−organic frameworks, CrystEngComm 18 (2016) 2596−2606, https://doi.org/10.1039/C6CE00371K.

[18] B. Fernández, G. Beobide, I. Sánchez, F. Carrasco-Marín, J.M. Seco, A.J. Calahorro, J. Cepeda, A. Rodríguez-Diéguez, Controlling interpenetration for tuning porosity and luminescence properties of flexible MOFs based on biphenyl-4,4′-dicarboxylic acid, CrystEngComm 18 (2016) 1282−1294, https://doi.org/10.1039/C5CE02036K.

[19] A.A. Garcıa Valdivia, M. Pérez Mendoza, D. Choquesillo-Lazarte, J. Cepeda, B. Fernández, M. Souto, M. González-Tejero, J.A. Garcıa, G.M. Espallargas, A. Rodrıguez Diéguez, Interpenetrated luminescent metal−organic frameworks based on 1 H -Indazole-5-carboxylic acid, Cryst. Growth Des. 20 (2020) 4550−4560, https://doi.org/10.1021/acs.cgd.0c00345.

[20] P.H. Cortés, Metal-organic frameworks in biomedical and environmental field. https://doi.org/10.1007/978-3-030-63380-6, 2021.

[21] L.E. Kreno, K. Leong, O.K. Farha, M.D. Allendorf, R.P. Van Duyne, J.T. Hupp, Metal−organic framework materials as chemical sensors, Chem. Rev. 112 (2012) 1105−1125, https://doi.org/10.1021/cr200324t.

[22] S.M. Cohen, Postsynthetic methods for the functionalization of metal-organic frameworks, Chem. Rev. 112 (2012) 970−1000, https://doi.org/10.1021/cr200179u.

[23] P. Falcaro, R. Ricco, C.M. Doherty, K. Liang, A.J. Hill, M.J. Styles, MOF positioning technology and device fabrication, Chem. Soc. Rev. 43 (2014) 5513−5560, https://doi.org/10.1039/C4CS00089G.

[24] A. Lendlein, R.S. Trask, Multifunctional materials: concepts, function-structure relationships, knowledge-based design, translational materials research, Multifunct. Mater. 1 (2018) https://doi.org/10.1088/2399-7532/aada7b, 0−5.

[25] S. Horike, S. Shimomura, S. Kitagawa, Soft porous crystals, Nat. Chem. 1 (2009) 695−704, https://doi.org/10.1038/nchem.444.

[26] J. Camarero, E. Coronado, Molecular vs. inorganic spintronics: the role of molecular materials and single molecules, J. Mater. Chem. 19 (2009) 1678−1684, https://doi.org/10.1039/b819594n.

O. Pajuelo-Corral, S. Pérez-Yáñez, I.J. Vitorica-Yrezabal et al.

Materials Today Chemistry 24 (2022) 100794

[27] J. Ferrer, V.M. García-Suárez, From microelectronics to molecular spintronics: an explorer's travelling guide, J. Mater. Chem. 19 (2009) 1696–1717, https://doi.org/10.1039/b810617g.

[28] E. Coronado, G. Mínguez Espallargas, Dynamic magnetic MOFs, Chem. Soc. Rev. 42 (2013) 1525–1539, https://doi.org/10.1039/C2CS35278H.

[29] A. Zabala-Lekuona, J.M. Seco, E. Colacio, Single-Molecule Magnets: from Mn12-ac to dysprosium metallocenes, a travel in time, Coord. Chem. Rev. 441 (2021) 213984, https://doi.org/10.1016/j.ccr.2021.213984.

[30] G. Mínguez Espallargas, E. Coronado, Magnetic functionalities in MOFs: from the framework to the pore, Chem. Soc. Rev. 47 (2018) 533–557, https://doi.org/10.1039/C7CS00653E.

[31] G.A. Craig, M. Murrie, 3D single-ion magnets, Chem. Soc. Rev. 44 (2015) 2135–2147, https://doi.org/10.1039/c4cs00439f.

[32] Y. Yu, X.M. Zhang, J.P. Ma, Q.K. Liu, P. Wang, Y. Bin Dong, Cu(i)-MOF: naked-eye colorimetric sensor for humidity and formaldehyde in single-crystal-to-single-crystal fashion, Chem. Commun. 50 (2014) 1444–1446, https://doi.org/10.1039/c3cc47723a.

[33] I. Ortiz-Gómez, A. Salinas-Castillo, A.G. García, J.A. Álvarez-Bermejo, I. de Orbe-Payá, A. Rodríguez-Diéguez, L.F. Capitán-Vallvey, Microfluidic paper-based device for colorimetric determination of glucose based on a metal-organic framework acting as peroxidase mimetic, Microchim. Acta 185 (2018) 47, https://doi.org/10.1007/s00604-017-2575-7.

[34] Y. Feng, Y. Wang, Y. Ying, Structural design of metal–organic frameworks with tunable colorimetric responses for visual sensing applications, Coord. Chem. Rev. 446 (2021) 214102, https://doi.org/10.1016/j.ccr.2021.214102.

[35] C.A. Redlich, W.S. Beckett, J. Sparer, K.W. Barwick, C.A. Riely, H. Miller, S.L. Sigal, S.L. Shalat, M.R. Cullen, Liver disease associated with occupational exposure to the solvent dimethylformamide, Ann. Intern. Med. 108 (1988) 680–686, https://doi.org/10.7326/0003-4819-108-5-680.

[36] R.P. Pohanish, Sittig's Handbook of Toxic and Hazardous Chemicals and Carcinogens, seventh ed., 2017.

[37] A.A. García-Valdivia, J.M. Seco, J. Cepeda, A. Rodríguez-Diéguez, Designing single-ion magnets and phosphorescent materials with 1-Methylimidazole-5-carboxylate and transition-metal ions, Inorg. Chem. 56 (2017) 13897–13912, https://doi.org/10.1021/acs.inorgchem.7b02020.

[38] A.A. García-Valdivia, S. Pérez-Yáñez, J.A. García, B. Fernández, J. Cepeda, A. Rodríguez-Diéguez, Magnetic and photoluminescent sensors based on metal-organic frameworks built up from 2-aminoisonicotinate, Sci. Rep. 10 (2020) 8843, https://doi.org/10.1038/s41598-020-65687-6.

[39] A. Rodríguez-Diéguez, S. Pérez-Yáñez, L. Ruiz-Rubio, J.M. Seco, J. Cepeda, From isolated to 2D coordination polymers based on 6-aminonicotinate and 3d-metal ions: towards field-induced single-ion-magnets, CrystEngComm 19 (2017) 2229–2242, https://doi.org/10.1039/c7ce00234c.

[40] O. Pajuelo-Corral, A. Zabala-Lekuona, E. San Sebastian, A. Rodríguez-Diéguez, J.A. García, L. Lezama, E. Colacio, J.M. Seco, J. Cepeda, Modulating magnetic and photoluminescence properties in 2-aminonicotinate-based bifunctional coordination polymers by merging 3d metal ions, Chem. Eur J. 26 (2020) 13484–13498, https://doi.org/10.1002/chem.202002755.

[41] S. Alvarez, D. Avnir, M. Llunell, M. Pinsky, Continuous symmetry maps and shape classification. The case of six-coordinated metal compounds, New J. Chem. 26 (2002) 996–1009, https://doi.org/10.1039/B200641N.

[42] V.A. Blatov, A.P. Shevchenko, D.M. Proserpio, Applied topological analysis of crystal structures with the program package topospro, Cryst. Growth Des. 14 (2014) 3576–3586, https://doi.org/10.1021/cg500498k.

[43] A. Spek, Structure validation in chemical crystallography, Acta Crystallogr. Sect. D. 65 (2009) 148–155, https://doi.org/10.1107/S090744490804362X.

[44] H.-Q. Hao, M.-X. Peng, Z.-Y. Chen, Poly[bis([mu]2-4-pyridinecarboxylato-[kappa]3N:O,O')cobalt(II)]: a triply interpenetrated structure with diamonoid topology, Acta Crystallogr. Sect. E. 63 (2007) m2605, https://doi.org/10.1107/S1600536807046314.

[45] Q.Q. Li, H. Liu, T.T. Zheng, P. Liu, J.X. Song, Y.Y. Wang, The effect of coordinated solvent molecules on metal coordination environments in single-crystal-to-single-crystal transformations, CrystEngComm 22 (2020) 6750–6775, https://doi.org/10.1039/d0ce01024c.

[46] D.-Q. Wu, D. Shao, X.-Q. Wei, F.-X. Shen, L. Shi, D. Kempe, Y.-Z. Zhang, K.R. Dunbar, X.-Y. Wang, Reversible on–off switching of a single-molecule magnet via a crystal-to-crystal chemical transformation, J. Am. Chem. Soc. 139 (2017) 11714–11717, https://doi.org/10.1021/jacs.7b07008.

[47] Y.-Q. Lan, H.-L. Jiang, S.-L. Li, Q. Xu, Solvent-induced controllable synthesis, single-crystal to single-crystal transformation and encapsulation of Alq3 for modulated luminescence in (4,8)-connected metal–organic frameworks, Inorg. Chem. 51 (2012) 7484–7491, https://doi.org/10.1021/ic202635a.

[48] J.I. Feldblyum, M. Liu, D.W. Gidley, A.J. Matzger, Reconciling the discrepancies between crystallographic porosity and guest access as exemplified by Zn-HKUST-1, J. Am. Chem. Soc. 133 (2011) 18257–18263, https://doi.org/10.1021/ja2055935.

[49] J. Thomas-Gipson, G. Beobide, O. Castillo, M. Fröba, F. Hoffmann, A. Luque, S. Pérez-Yáñez, P. Román, Paddle-wheel shaped copper(II)-adenine discrete entities as supramolecular building blocks to afford porous supramolecular metal-organic frameworks (SMOFs), Cryst. Growth Des. 14 (2014) 4019–4029, https://doi.org/10.1021/cg500634y.

[50] K. Sumida, D.L. Rogow, J.A. Mason, T.M. McDonald, E.D. Bloch, Z.R. Herm, T.H. Bae, J.R. Long, Carbon dioxide capture in metal-organic frameworks, Chem. Rev. 112 (2012) 724–781, https://doi.org/10.1021/cr2003272.

[51] R. Aniruddha, I. Sreedhar, B.M. Reddy, MOFs in carbon capture-past, present and future, J. CO2 Util. 42 (2020) 101297, https://doi.org/10.1016/j.jcou.2020.101297.

[52] H. Pan, J.A. Ritter, P.B. Balbuena, Examination of the approximations used in determining the isosteric heat of adsorption from the Clausius-Clapeyron equation, Langmuir 14 (1998) 6323–6327, https://doi.org/10.1021/la9803373.

[53] S. Geng, E. Lin, X. Li, W. Liu, T. Wang, Z. Wang, D. Sensharma, S. Darwish, Y.H. Andaloussi, T. Pham, P. Cheng, M.J. Zaworotko, Y. Chen, Z. Zhang, Scalable room-temperature synthesis of highly robust ethane-selective metal−organic frameworks for efficient ethylene purification, J. Am. Chem. Soc. (2021), https://doi.org/10.1021/jacs.1c02108.

[54] O.T. Qazvini, R. Babarao, Z.L. Shi, Y.B. Zhang, S.G. Telfer, A robust ethane-trapping metal-organic framework with a high capacity for ethylene purification, J. Am. Chem. Soc. 141 (2019) 5014–5020, https://doi.org/10.1021/jacs.9b00913.

[55] B. Zhu, J.W. Cao, S. Mukherjee, T. Pham, T. Zhang, T. Wang, X. Jiang, K.A. Forrest, M.J. Zaworotko, K.J. Chen, Pore engineering for one-step ethylene purification from a three-component hydrocarbon mixture, J. Am. Chem. Soc. 143 (2021) 1485–1492, https://doi.org/10.1021/jacs.0c11247.

[56] P.Q. Liao, W.X. Zhang, J.P. Zhang, X.M. Chen, Efficient purification of ethene by an ethane-trapping metal-organic framework, Nat. Commun. 6 (2015) 8697, https://doi.org/10.1038/ncomms9697.

[57] L. Xu, C.-Y. Xing, D. Ke, L. Chen, Z.-J. Qiu, S.-L. Zeng, B.-J. Li, S. Zhang, Amino-functionalized β-cyclodextrin to construct green metal−organic framework materials for CO2 capture, ACS Appl. Mater. Interfaces 12 (2020) 3032–3041, https://doi.org/10.1021/acsami.9b20003.

[58] S. Couck, J.F.M. Denayer, G.V. Baron, T. Rémy, J. Gascon, F. Kapteijn, An amine-functionalized MIL-53 Metal−Organic framework with large separation power for CO2 and CH4, J. Am. Chem. Soc. 131 (2009) 6326–6327, https://doi.org/10.1021/ja900555r.

[59] Y. Ye, H. Zhang, L. Chen, S. Chen, Q. Lin, F. Wei, Z. Zhang, S. Xiang, Metal-−organic framework with rich accessible nitrogen sites for highly efficient CO2 capture and separation, Inorg. Chem. 58 (2019) 7754–7759, https://doi.org/10.1021/acs.inorgchem.9b00182.

[60] Z. Zhang, Z.-Z. Yao, S. Xiang, B. Chen, Perspective of microporous metal−organic frameworks for CO2 capture and separation, Energy Environ. Sci. 7 (2014) 2868–2899, https://doi.org/10.1039/C4EE00143E.

[61] E.J. Carrington, C.A. McAnally, A.J. Fletcher, S.P. Thompson, M. Warren, L. Brammer, Solvent-switchable continuous-breathing behaviour in a diamondoid metal−organic framework and its influence on CO2 versus CH4 selectivity, Nat. Chem. 9 (2017) 882–889, https://doi.org/10.1038/nchem.2747.

[62] N.F. Chilton, R.P. Anderson, L.D. Turner, A. Soncini, K.S. Murray, PHI: a powerful new program for the analysis of anisotropic monomeric and exchange-coupled polynuclear d- and f-block complexes, J. Comput. Chem. 34 (2013) 1164–1175, https://doi.org/10.1002/jcc.23234.

[63] F. Lloret, M. Julve, J. Cano, R. Ruiz-García, E. Pardo, Magnetic properties of six-coordinated high-spin cobalt(II) complexes: theoretical background and its application, Inorganica Chim. Acta 361 (2008) 3432–3445, https://doi.org/10.1016/j.ica.2008.03.114.

[64] R.F. Higgins, B.N. Livesay, T.J. Ozumerzifon, J.P. Joyce, A.K. Rappé, M.P. Shores, A family of related Co(II) terpyridine compounds exhibiting field induced single-molecule magnet properties, Polyhedron 143 (2018) 193–200, https://doi.org/10.1016/j.poly.2017.10.008.

[65] H. Wu, L. Gao, J. Zhang, L. Zhai, T. Gao, X. Niu, T. Hu, Syntheses, characterization, and slow magnetic relaxation or luminescence properties of three new 2D coordination polymers, J. Mol. Struct. 1219 (2020) 128613, https://doi.org/10.1016/j.molstruc.2020.128613.

[66] R. Herchel, L. Váhovská, I. Potočňák, Z. Trávníček, Slow magnetic relaxation in octahedral cobalt(II) field-induced single-ion magnet with positive axial and large rhombic anisotropy, Inorg. Chem. 53 (2014) 5896–5898, https://doi.org/10.1021/ic500916u.

[67] Y.-F. Deng, M.K. Singh, D. Gan, T. Xiao, Y. Wang, S. Liu, Z. Wang, Z. Ouyang, Y.-Z. Zhang, K.R. Dunbar, Probing the axial distortion effect on the magnetic anisotropy of octahedral Co(II) complexes, Inorg. Chem. 59 (2020) 7622–7630, https://doi.org/10.1021/acs.inorgchem.0c00531.

[68] F. Neese, Software update: the ORCA program system, version 4.0, WIREs Comput. Mol. Sci. 8 (2018) e1327, https://doi.org/10.1002/wcms.1327.

[69] J. Titiš, R. Boča, Magnetostructural D correlations in hexacoordinated cobalt(II) complexes, Inorg. Chem. 50 (2011) 11838–11845, https://doi.org/10.1021/ic202108j.

[70] J.M. Zadrozny, J. Liu, N.A. Piro, C.J. Chang, S. Hill, J.R. Long, Slow magnetic relaxation in a pseudotetrahedral cobalt(ii) complex with easy-plane anisotropy, Chem. Commun. 48 (2012) 3927–3929, https://doi.org/10.1039/C2CC16430B.

[71] A.K. Mondal, A. Mondal, S. Konar, Slow magnetic relaxation in a one-dimensional coordination polymer constructed from hepta-coordinate cobalt(II) nodes, Magnetochemistry 6 (2020) 45, https://doi.org/10.3390/magnetochemistry6040045.

[72] M.K. Singh, P. Shukla, M. Khatua, G. Rajaraman, A design criteria to achieve giant ising-type Anisotropy in CoII-encapsulated metallofullerenes, Chem. Eur J. 26 (2020) 464–477, https://doi.org/10.1002/chem.201903618.

[73] B. Yao, M.K. Singh, Y.F. Deng, Y.N. Wang, K.R. Dunbar, Y.Z. Zhang, Trigonal prismatic cobalt(II) single-ion magnets: manipulating the magnetic relaxation

through symmetry control, Inorg. Chem. 59 (2020) 8505−8513, https://doi.org/10.1021/acs.inorgchem.0c00950.

[74] A. Sarkar, S. Tewary, S. Sinkar, G. Rajaraman, Magnetic anisotropy in CoIIX4 (X=O, S, Se) single-ion magnets: role of structural distortions versus heavy atom effect, Chem. Asian J. 14 (2019) 4696−4704, https://doi.org/10.1002/asia.201901140.

[75] J.M. Frost, K.L.M. Harriman, M. Murugesu, The rise of 3-d single-ion magnets in molecular magnetism: towards materials from molecules? Chem. Sci. 7 (2016) 2470−2491, https://doi.org/10.1039/c5sc03224e.

[76] A. Sarkar, S. Dey, G. Rajaraman, Role of coordination number and geometry in controlling the magnetic anisotropy in FeII, CoII, and NiII single-ion magnets, Chem. Eur J. 26 (2020) 14036−14058, https://doi.org/10.1002/chem.202003211.

[77] T.T. Da Cunha, V.M.M. Barbosa, W.X.C. Oliveira, E.F. Pedroso, D.M.A. Garciá, W.C. Nunes, C.L.M. Pereira, Field-induced slow magnetic relaxation of a six-coordinate mononuclear manganese(II) and cobalt(II) oxamate complexes, Inorg. Chem. 59 (2020) 12983−12987, https://doi.org/10.1021/acs.inorgchem.0c01628.

[78] X.Q. Wei, D. Shao, C.L. Xue, X.Y. Qu, J. Chai, J.Q. Li, Y.E. Du, Y.Q. Chen, Field-induced slow magnetic relaxation in two interpenetrated cobalt(ii) metal-organic framework isomers, CrystEngComm 22 (2020) 5275−5279, https://doi.org/10.1039/d0ce00979b.

[79] Y. Yu, J.-P. Ma, C.-W. Zhao, J. Yang, X.-M. Zhang, Q.-K. Liu, Y.-B. Dong, Copper(I) metal−organic framework: visual sensor for detecting small polar aliphatic volatile organic compounds, Inorg. Chem. 54 (2015) 11590−11592, https://doi.org/10.1021/acs.inorgchem.5b02150.